Applied Catalysis B: Environment and Energy 344 (2024) 123664

Contents lists available at ScienceDirect

Applied Catalysis B: Environment and Energy

journal homepage: www.elsevier.com/locate/apcatb

Synergistic mechanism of hetero-interfacial oxygen vacancies on catalytic oxidation of 1,2-dichloroethane over Ru-modified monolayer-dispersed WO_x/CeO_2 catalysts: Differences in distribution of active sites

Xinyu Meng [a], Qirui Wang [a], Wei Wang [a,*], Tiantian Zhang [a], Yan Sun [a], Yuliang Shi [a], Shuiliang Yao [a,*], Zuliang Wu [a], Jing Li [a], Erhao Gao [a], Jiali Zhu [a], Qiguang Dai [b,*]

[a] School of Environmental Science and Engineering, Changzhou University, Jiangsu 213164, PR China
[b] State Key Laboratory of Green Chemical Engineering and Industrial Catalysis, Research Institute of Industrial Catalysis, School of Chemistry and Molecular Engineering, East China University of Science and Technology, Shanghai 200237, PR China

ARTICLE INFO

Keywords:
1,2-dichloroethane
Catalytic oxidation
Hetero-interfacial oxygen vacancies
Redox–acid sites
Synergistic effects

ABSTRACT

Ru-modified monolayer-dispersed WO_x/CeO_2 hybrid composites were prepared by co-impregnation (CI) and step impregnation (SI) methods, and the effects of active site distribution on the catalytic oxidation of 1,2-dichloroethane (DCE) were investigated. Ru species tends to be deposited on the monolayer-dispersed WO_x (m-WO_x) by SI method, which can increase the oxygen vacancies ($O_{V,m\text{-}WOx}$) at m-WO_x/CeO_2 interfaces. Abundant $O_{V,m\text{-}WOx}$ can promote the formation of more active W–OH and accelerate the dechloridation and oxydehydrogenation of DCE. Oppositely, for CI method, Ru species exists mainly in the form of Ru−O−Ce bonds, increasing the oxygen vacancies ($O_{V,RuCe}$) into CeO_2 surface lattices and promoting the deep oxidation of intermediate products. The closer contact between the two hetero-interfacial oxygen vacancies ($O_{V,RuCe}$ and $O_{V,m\text{-}WOx}$) on Ru-modified m-WO_x/CeO_2 produces a stronger synergistic effect on DCE activation and oxidation, and meanwhile advantageously inhibits the adsorption of chlorine species as well as the formation of polychlorinated by-products.

1. Introduction

As a kind of indispensable organic solvent and intermediate in industrial production, chlorinated volatile organic compounds (CVOCs) have seriously harmed the atmospheric environment and human health due to their severe toxicity, low biodegradability, and high chemical stability [1,2]. In recent years, some environmental regulations have increasingly restricted the CVOCs emissions in China, so there is an urgent need to develop economically viable methods of eliminating CVOCs. Catalytic oxidation is considered to be one of the most cost-effective technologies for CVOCs removal [2]. Cerium oxide (CeO_2) with the excellent redox ability and rapid oxygen storage/release capacity is deemed as a promising candidate for catalytic oxidation of CVOCs [3]. However, the pristine CeO_2 is easily deactivated due to the inorganic chlorine (Cl) species strongly occupying on surface oxygen vacancies [4].

The Cl_2 formation via Deacon reaction is an effective migration pathway of Cl species on CeO_2 surfaces, and Deacon reaction usually depends on the mobility of surface lattice oxygen of CeO_2 [4]. The increased mobility of surface lattice oxygen can be implemented by the doping of transition metal ions (Fe [5], Mn [6], Co [7]) or loading of precious metals (Ru [8], Pt [9], Pd [10]). Among these modification methods, Ru loading can be deemed as the most promising candidate because RuO_2 is the main active component of catalyst for industrial Deacon reaction [11]. Nonetheless, the high redox property (or high Deacon reactivity) of RuO_x/CeO_2, inevitably leads to the formation of abundant Cl_2, promoting the further chlorination to generate more polychlorinated organics during the CVOCs catalytic oxidation [12]. In addition, the HCl desorption assisted by Brönsted acid sites (B acids) is another effective way to enhance the Cl tolerance of CeO_2 [4], including the introduction of WO_x [13], VO_x [14], MoO_x [15], molecular sieves [16], H_xPO_4 [17] and so on. Unfortunately, excessive acid sites can cover the redox sites and weaken the deep oxidation capacity of CeO_2-based catalysts, easily causing the coking on surfaces [18]. Therefore, a well-designed CeO_2-based catalyst for catalytic oxidation of CVOCs should be abundant in both redox and acid sites. The rational regulation between redox ability (especially for Ru modification) and acidity with better synergistic effects imparted excellent activity,

* Corresponding authors.
E-mail addresses: ww130920@cczu.edu.cn (W. Wang), yaos@cczu.edu.cn (S. Yao), daiqg@ecust.edu.cn (Q. Dai).

https://doi.org/10.1016/j.apcatb.2023.123664
Received 22 September 2023; Received in revised form 13 December 2023; Accepted 24 December 2023
Available online 25 December 2023
0926-3373/© 2023 Elsevier B.V. All rights reserved.

selectivity and durability to CeO_2, such as RuO_x–H_xPO_4/CeO_2 [19], RuO_x–SnO_x/CeO_2 [20] and RuO_x–HZSM-5/CeO_2 [21]. However, for such three-phase systems, the distribution positions and structure/electron effects of various active centers can significantly influence the ways of synergy between redox and acid sites on CeO_2 surfaces. Taking RuO_x–WO_x/CeO_2 as an example, Ru species can be distributed on either WO_x surfaces or CeO_2 surfaces (or even WO_x/CeO_2 interfaces). The different distribution sites of Ru greatly influence the amounts/types/ functions/electronic structures of redox sites (RuO_x) and acid sites (WO_x), subsequently changing the reaction paths of CVOCs catalytic oxidation over CeO_2-based catalysts.

This study proposed some new mechanistic insights into the synergistic effects between redox and acid sites for CVOCs catalytic oxidation over Ru-modified monolayer-dispersed WO_x/CeO_2 catalysts. 1,2-dichloroethane (DCE) was utilized as a representative probe molecule of CVOCs in our study. DCE is generally emitted from the waste streams in chemical plants, chlor-alkali and pharmaceutical industries [3,4], and the distributions of its intermediate products during the catalytic oxidation can availably reflect more information about surface properties of catalysts [20]. The different impregnation methods made a great difference in the distribution states of Ru species and redox−acid sites. The relationship between the two interfacial oxygen vacancies and redox ability/acidity were determined, and their synergistic ways affected by impregnation methods were investigated in detail through a series of experimental and computational methods. Such a study may provide valuable guidance for rational regulation between redox ability and acidity on CeO_2-based catalysts for effective CVOCs elimination.

2. Experimental section

2.1. Catalyst preparation

CeO_2 supports with the nanoplate morphology were synthesized by a solvothermal method, as reported by our pervious study [22]. All supported CeO_2-based catalysts were obtained by an incipient-wetness impregnation method. 1Ru–xW/CeO_2–CI catalysts were prepared by a co-impregnation (CI) of as-synthesized CeO_2 (0.5 g) with the mixed solution of $RuCl_3$ and $(NH_4)_6H_2W_{12}O_{40}$. The catalysts were denoted as 1Ru–xW where 1 represented the weight percent (wt%) of Ru, and xW (x = 1, 3, 10, 15) represented the weight percent (wt%) of W on CeO_2. For example, 1Ru–10 W/CeO_2 referred to 1 wt% Ru and 10 wt% W on CeO_2 supports. Similarly, 1Ru–xW/CeO_2–SI catalysts were prepared by a step impregnation (SI) method. First, xW/CeO_2 (x = 1, 3, 10, 15) catalysts were prepared, and then 1 wt% Ru continued to be loaded on the as-synthesized xW/CeO_2. The 1Ru/CeO_2 and 1Ru/WO_3 were also prepared for comparison, and the WO_3 supports was synthesized by the direct pyrolysis of $(NH_4)_6H_2W_{12}O_{40}$. All impregnated solids were dried at 80 ℃ for 12 h and finally calcined at 450 °C in air for 120 min. The actual Ru and W loadings (ICP−OES results, Table S1) of 1Ru/CeO_2, 10 W/CeO_2, 1Ru–10 W/CeO_2–CI and 1Ru–10xW/CeO_2–SI were closed to their theoretical values.

2.2. Catalyst characterization and DFT calculation

The crystal structures, surface properties and electronic structures of the as-prepared catalysts were measured using a series of characterization methods. And the DFT calculations were carried out by using the Vienna ab-initio simulation package (VASP). Details were illustrated in the Supporting Information.

2.3. Catalyst evaluation

In a continuous-flow fixed-bed quartz microreactor (5 mm inner diameter), the catalytic oxidation of 1,2-dichloroethane (DCE) was performed. 200 mg grain catalyst (40–60 mesh) was packed on a quartz sieve in the middle of the quartz microreactor. The concentration of DCE was 1200 ppm (volume fraction) or 1000 mg m^{-3}, and the total flow rate of 20% O_2 and 80% N_2 was 100 mL min^{-1} (weight hourly space velocity (WHSV) = 30,000 mL g^{-1} h^{-1}). Under wet condition, 3.0 vol% water vapor was introduced into the reaction system described above. The outlet gases were analyzed using a gas chromatograph with a CO_2 transfer furnace and flame ionization detector. The detected by-products included vinyl chloride (VC), dichloroethylene, trichloroethylene (TCE), trichloroethane (TCA), perchloroethylene (PCE) and tetrachloroethane (TeCA). The specific calculation methods of DCE conversion and CO_2 selectivity were exhibited in the Supporting Information.

3. Results and discussion

3.1. Crystal structure, morphology and composition

The XRD patterns of Ru–W/CeO_2 catalysts were shown in Fig. 1**a**. All CeO_2-based catalysts showed the same characteristic diffraction peaks assigned to the face-centered-cubic (FCC) CeO_2 (PDF# 78–0694, Fig. 1**a**), and no characteristic diffraction peaks of the supported Ru or W species were detected, indicating that Ru or W species existed in the form of solid solutions or highly-dispersed nanoparticles [22,23]. For 1Ru–CeO_2, its diffraction angle of CeO_2 (220) plane shifted to the lower value, resulting in a slight lattice expansion of FCC structure (**α,** Table S1). This was mainly due to the fact that Ru ions were easily incorporated into CeO_2 lattices, and the doping effect could stimulate the production of more Ce^{3+}. Noticeably, the ion radius of Ce^{3+} (1.23 Å) is larger than that of Ce^{4+} (0.97 Å) [22,24]. The W loading could reduce the specific surface area and pore volume of CeO_2 (**S_{BET}** and **V_{pore}**, Table S1) due to the highly dispersed W species blocking the pore channels [24]. The detailed structural and physical parameters of these CeO_2-based catalysts were exhibited in Table S1 and Fig. S1.

Fig. 1**b** displayed the Raman spectra of different CeO_2-based catalysts. The intense band of CeO_2 at approximately 467 cm^{-1} was attributed to the F_{2g} symmetry mode of FCC structure [22]. The introduction of both W and Ru species could cause a red shift of F_{2g} symmetry mode (467 cm^{-1}) due to the lattice distortion from the effect of hetero-ion doping [24,25]. For 10 W–CeO_2, the weak bands at 712 and 806 cm^{-1} were attributed to the W–O–W vibration modes of WO_3 crystal species (Fig. 1**b** and Fig. S2), while the evident band at 971 cm^{-1} was ascribed to the monotungstate monoxo WO_5(O═W(–O–Ce)$_4$) [24,26]. This also indicated that the W species was dominated by a monolayer coverage (m-WO_x) on CeO_2 surfaces [24,26–28]. For 1Ru–CeO_2, the characteristic bands assigned to the separated RuO_x species were not detectable, and only two bands at 695 and 968 cm^{-1} ascribed to the Ru–O–Ce bonds appeared due to the substitution of Ru ions to the lattice Ce ions (XRD results) [25,29]. The Ru–O–Ce bonds in CeO_2 surface lattices could promote the formation of oxygen vacancies (O_V). Herein, we referred to the O_V due to the role of Ru−O−Ce as $O_{V,RuCe}$ for short. Importantly, for the bimetal supported CeO_2 catalysts (1Ru–10 W/CeO_2–SI and 1Ru–10 W/CeO_2–CI), a newly broad band at 920 cm^{-1} could belong to the monotungstate dioxo WO_4((O=)$_2$W(O–M)$_2$) species [24,26,28]. Relative to monotungstate monoxo WO_5, monotungstate dioxo WO_4 possessed more loss of coordinated oxygen, and that was to say more O_V. Similarly, we referred to this O_V on the supported m-WO_x as $O_{V,m\text{-}WOx}$ for short. Relative to 1Ru–10 W/CeO_2–CI, 1Ru–10 W/CeO_2–SI possessed the higher band intensity of monotungstate dioxo WO_4 (920 cm^{-1}), indicating that it had more $O_{V,m\text{-}WOx}$. However, 1Ru–10 W/CeO_2–CI still showed the visible band at 695 cm^{-1}, demonstrating its more Ru–O–Ce bonds.

The morphology and surface composition of Ru–W/CeO_2 catalysts were confirmed by SEM, EDX spectra and TEM/HRTEM, and the specific analyses were exhibited in the section of "**Crystal structure, morphology and composition**" in Supporting Information (Fig. S3-S7). However, for the bimetal supported CeO_2 catalysts, there was no information about the lattice diffractions (FFT patterns) and lattice fringe spacing of W or Ru species on their HRTEM images (Fig. S6c **and**

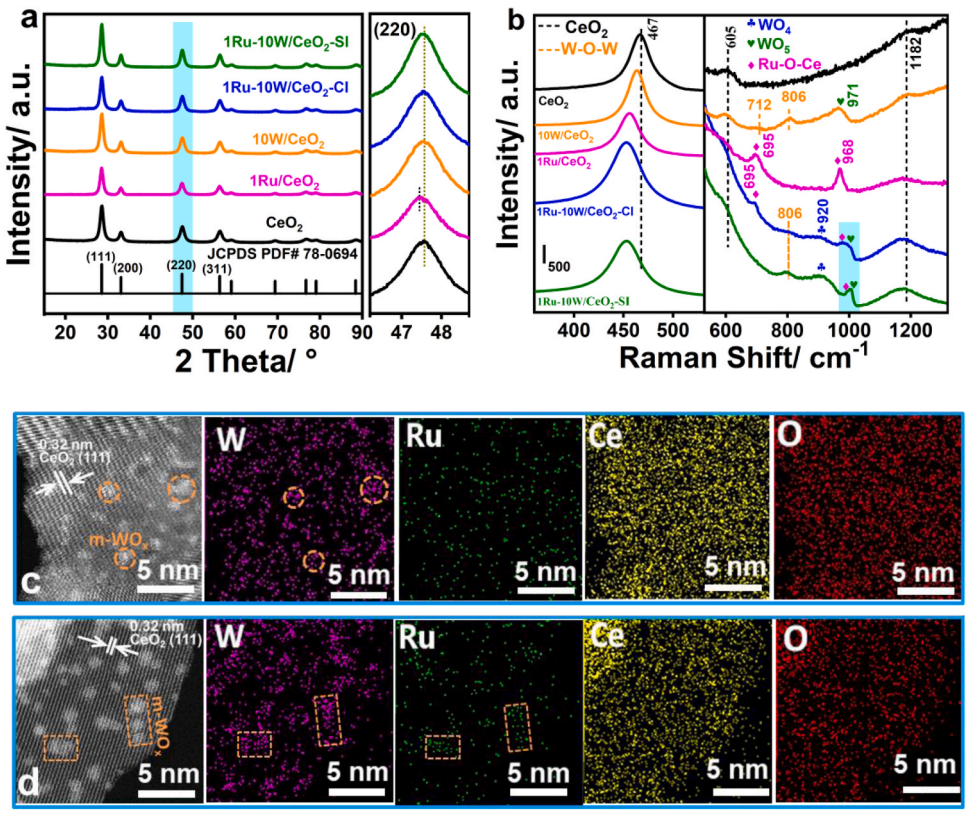

Fig. 1. (a) XRD patterns, (b) Raman spectra of various CeO_2-based catalysts, and selected STEM images and corresponding EDX mappings of (c) 1Ru–10 W/CeO_2–CI and (d) 1Ru–10 W/CeO_2–SI.

Fig. S7c). Therefore, the scanning transmission electron microscopy (STEM) and the corresponding EDX mappings were performed to further determine the existence forms of W and Ru species on CeO_2 surfaces (Fig. 1**c,d**). Obviously, for both 1Ru–10 W/CeO_2–CI and 1Ru–10 W/CeO_2–SI catalysts, W was mainly dispersed in the form of WO_x nanoclusters (< 2 nm) on CeO_2 surfaces, and this was in agreement with a monolayer coverage of WO_x (m-WO_x) in Raman results. The intense interface interaction between WO_x nanoclusters and CeO_2 supports could result in the formation of W−O−Ce or $O_{V,m\text{-}WOx}$ [24,26]. No Ru ensembles were observed in the STEM images (low distribution density), with only CeO_2 lattice fringes observed (Fig. 1**c,d**). This is because there is little contrast between the atomic numbers of Ru (Z = 44) and Ce (Z = 58), which significantly limits the visualization of Ru atoms on CeO_2 surfaces [30]. However, the electron energy loss spectroscopy (EELS) could detect the signal of Ru−M−edge (close to 279 eV) in Fig. S6d and Fig. S7d. These results indicated that the Ru was well mixed into the CeO_2 lattices or m-WO_x lattices [23]. For comparison, Ru distribution was more concentrated in the locations of WO_x nanoclusters in the EDX mappings of 1Ru–10 W/CeO_2–SI (Fig. 1**d**), demonstrating that Ru species were more likely to be incorporated into m-WO_x lattices by SI method. In contrast, Ru species was evenly distributed over all the imaged CeO_2 particles of 1Ru–10 W/CeO_2–CI (Fig. 1**c**). Combined with the more obvious Ru–O–Ce signal (695 cm^{-1}, Fig. 1**b**) in Raman spectrum of 1Ru–10 W/CeO_2–CI, it could be inferred that Ru was easily doped into the CeO_2 surface lattices by CI method.

3.2. Surface electronic structure

Fig. 2**a** showed the UV–Vis DRS spectra of these supported CeO_2 catalysts. It was evident that all CeO_2-based catalysts had two intense absorption bands at 275 and 345 nm, corresponding to the overlapping of O^{2-}→Ce^{4+} charge transfer and interband transition, respectively [25]. Compared with the 10 W/CeO_2, Ru loading could enhance the absorption of the catalysts in the visible region, which was attributed to the surface plasmon resonance (SPR) of Ru species [25,30]. It is well known that the difference in the peak values generally depends on the sizes, valence states and chemical environments of Ru species [25]. The absorption peak value of Ru species in 1Ru–10 W/CeO_2–CI (514 nm) were closed to that in 1Ru/CeO_2 (499 nm), while the one in 1Ru–10 W/CeO_2–SI exhibited the same range (650–750 nm) as that in 1Ru/WO_3 catalyst (Fig. S8). This further indicated that more Ru species could closely contact with CeO_2 surfaces by CI method, while it was preferentially deposited on m-WO_x by SI method. Relative to pure CeO_2, the lower band gap of 1Ru/CeO_2 was mainly assigned to the effect of O_V by Ru-doping [32]. On the contrary, the slightly increased band gap of 10 W/CeO_2 was related to the stronger electronegativity of modified W ions (W–O–Ce bonds), preventing the electron transfer from the O_{2p} to Ce_{4f} bands [31]. In addition, the bimetal supported CeO_2 catalysts were assigned the band gaps between those of 10 W/CeO_2 and 1Ru/CeO_2 (Fig. 2**b**). This well confirmed that W and Ru loading had an opposite electronic effects on CeO_2 supports [31]. In PL emission spectra (Fig. 2**c**), a broad band located from 420 to 540 nm with a maximum (470 nm) is attributed to the 5d− 4 f ($5d^1 \rightarrow 4f^1$) transition of Ce^{3+} ions [33]. This stronger emission band of 1Ru/CeO_2 confirmed the Ru–O–Ce bonds could promote the formation of Ce^{3+}. Nonetheless, this band was very weak for 10 W/CeO_2 catalyst, because the lattice relaxation of CeO_2 by W modification may induce the oxidation of Ce^{3+} to Ce^{4+}, indicating an inhibiting effect of W–O–Ce bonds on the formation of surface Ce^{3+} [31].

We further investigated the surface charge properties by zeta potential measurements (Fig. 2**d**). The zeta potential of pure CeO_2 in distilled water (pH=7) was about − 0.86 mV [34], while the positive charge on 1Ru/CeO_2 surfaces (4.96 mV) was mainly attributed to the abundant $O_{V,RuCe}$ [35]. The positively charged surfaces could promote the adsorption of anionic species [34], such as Cl^- ions. In contrast, 10 W/CeO_2 exhibited a negative potential (−1.14 mV), mainly resulting

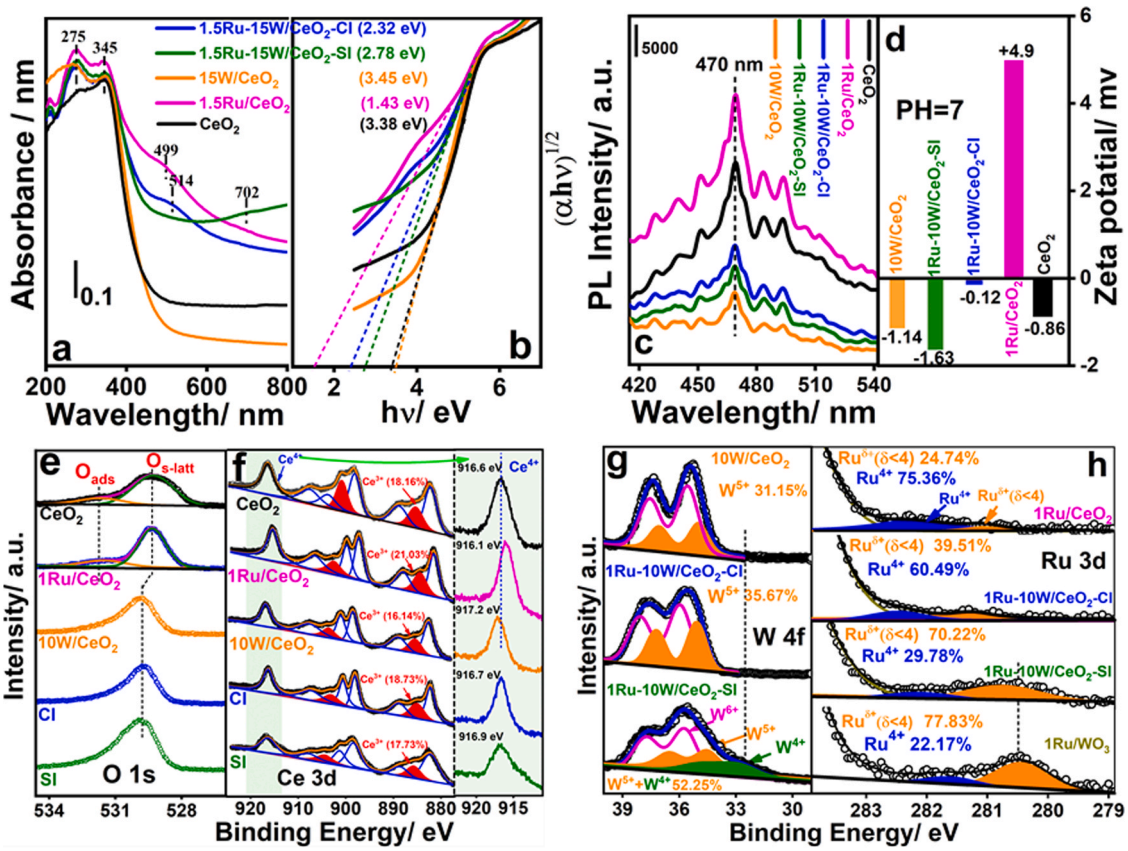

Fig. 2. . (a,b) UV–Vis diffuse reflectance spectra (DRS) and the corresponding Tauc plots for the band gap calculations, (c) Photoluminescence (PL) emission spectra, (d) Zeta potential measurements, and (e–h) XPS spectra of O 1 s, Ce 3d, W 4 f and Ru 3d of various catalysts.

from the terminal electron-rich W═O$^{\delta-}$ bonds on monotungstate monoxo WO_5 [36]. The formation of W═O unsaturated bonds was related to the missing coordinated oxygen ($O_{V,m\text{-}WOx}$) of surface W ions [27,28]. The zeta potential of 1Ru–10 W/CeO_2–CI (−0.12 mV) were between that of 1Ru/CeO_2 and 10 W/CeO_2 due to the common influences of $O_{V,RuCe}$ and electron-rich W═O$^{\delta-}$ bonds. But the relatively lower value for 1Ru–10 W/CeO_2–SI (−1.63 mV) could be linked with the more electron-rich W═O$^{\delta-}$ bonds, such as the highly-unsaturated $^{\delta-}$O═W═O$^{\delta-}$ from monotungstate dioxo WO_4 (Raman results), which also represented more $O_{V,m\text{-}WOx}$ on its surfaces.

XPS spectra of Ce 3d, O 1 s, W 4 f and Ru 3d for these Ru/W-CeO_2 samples were shown in Fig. 2**e-h**. Pure CeO_2 and 1Ru/CeO_2 showed the obvious peaks of surface absorbed oxygen (O_{ads}, Fig. 2**e**), which were attributed to the O_2 activation on $O_{V,RuCe}$ [22,25]. However, this O_{ads} peak became indistinct, and the peak values (binding energies) of surface lattice oxygen ($O_{s\text{-}latt}$) were positively shifted after W modification, increasing the barrier of oxygen escaping from CeO_2 surface lattices [37]. The surface relative concentrations of Ce^{3+} were estimated by the ratios of integral areas ($A_{Ce3+}/(A_{Ce3+}+A_{Ce4+})$), and the results followed the sequence of 1Ru–CeO_2 > 1Ru–10 W/CeO_2–CI > 1Ru–10 W/CeO_2–SI > 10 W/CeO_2 (Fig. 2**f**). Deng et al. found that the substitution of high-valent Ta^{5+} donated more coordination oxygen than Ce^{4+} or Ce^{3+}, and this inhibited the formation of surface O_V of CeO_2 [38]. Similarly, the substitution of high-valent W^{6+} could also cause this negative effect by W–O–Ce bonds ($W^{6+} + Ce^{3+} \rightarrow Ce^{4+} + W^{5+}$), thus reducing the $O_{V,RuCe}$ (PL results). In addition, relative to pure CeO_2 (916.6 eV), the binding energy of Ce^{4+} 3d in 1Ru/CeO_2 (916.1 eV) shifted to the lower value, but 10 W/CeO_2 exhibited a higher binding energy of Ce^{4+} 3d (917.2 eV), further demonstrated that the W and Ru modifications could have an opposite electronic effect on CeO_2 surfaces (PL and UV–Vis DRS results).

However, the W–O–Ce bonds could increase the unsaturated coordination of W^{6+} ions reversely, resulting in the formation of lower-valent W ions [24]. The appearance of surface W^{5+} over 10 W/CeO_2 and 1Ru–10 W/CeO_2–CI further demonstrated the above viewpoints (Fig. 2**g**). And even the W^{4+} ions with the highly-unsaturated coordination were detected in the W 4 f XPS spectra of 1Ru–10 W/CeO_2–SI [39]. For 1Ru–10 W/CeO_2–SI catalyst, the appearance of W^{4+} and highest relative content of W^{5+}+W^{4+} (51.25%) represented the large concentrations of $O_{V,m\text{-}WOx}$ at m-WO_x/CeO_2 interfaces (Raman and zeta potential results). The distribution sites of Ru species could be strongly identified by Ru 3d XPS spectra (Fig. 2**h**). Evidently, the Ru species on 1Ru/CeO_2 and 1Ru–10 W/CeO_2–CI surfaces were prominently existed as the Ru^{4+}. The Ru^{4+} ions possessed a preference for insertion into the CeO_2 lattices, which could induce the increase of $O_{V,RuCe}$ [39]. However, the Ru species on 1Ru–10 W/CeO_2–SI surfaces consisted largely of low-valent $Ru^{\delta+}$ ($\delta < 4$), which was in agreement with the dominating peak of $Ru^{\delta+}$ in Ru/WO_3 catalyst (Fig. 2**h**) [39–42]. This further demonstrated that the main landing sites of Ru species were the supported m-WO_x species rather than CeO_2 surfaces by SI method (STEM and UV-Vis results). According to the previous literatures [43–45], Ru modification could favorably generate the O_V on WO_x surfaces by Ru–O–W linkages. Therefore, the abundant $O_{V,m\text{-}WOx}$ for 1Ru–10 W/-CeO_2–SI was a result of combined action of Ru−O−W and W−O−Ce (or possible Ru−O−W−O−Ce) at Ru-modified m-WO_x/CeO_2 interfaces.

Based on the structural and electronic analyses of these supported CeO_2 catalysts, a structural model with various atoms doped CeO_2 (111) planes were built for calculation (Fig. S9 **and** Fig. 3). The differential charge density profile of Ru–CeO_2 (111) revealed the electron loss of partial O atoms after Ru doping (Fig. 3**a,** red dashed lines), which could reduce the bond energy of Ce–O, facilitating the escape of $O_{s\text{-}latt}$ to form $O_{V,RuCe}$. Meanwhile, the electron transfer occurred from Ru atom to Ce

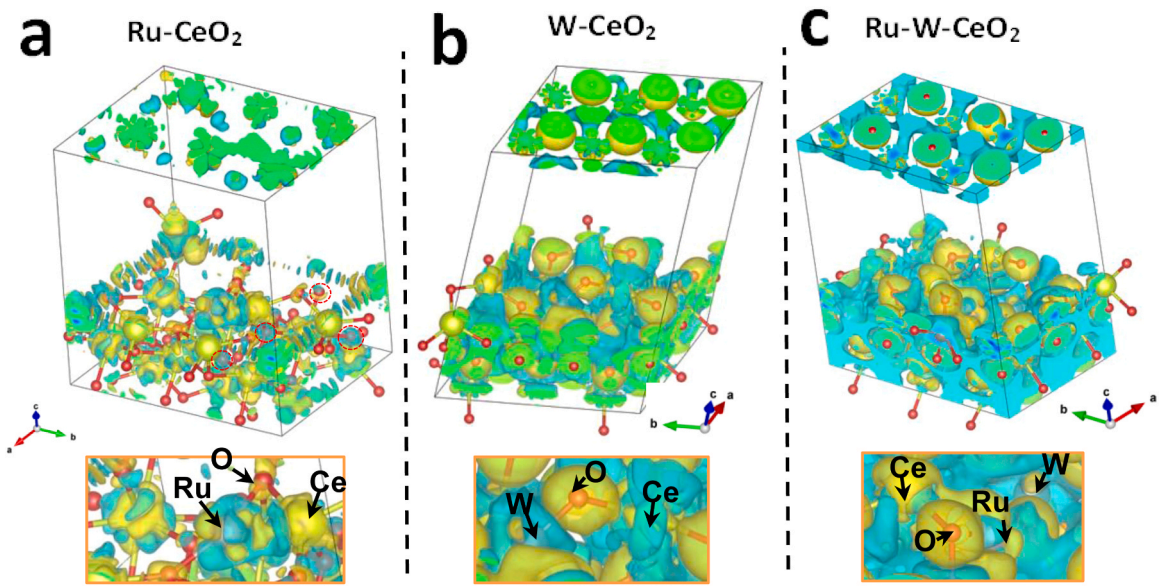

Fig. 3. The isosurfaces of charge density differences for the Ru-doped CeO_2 (111), W-doped CeO_2 (111), and Ru,W co-doped CeO_2 (111). Note: the yellow and blue colors revealed charge accumulation and depletion, respectively.

atom by Ru–O–Ce bonds in favor of more Ce^{3+} formed (PL and XPS results) [46]. The surface of Ru–CeO_2 was proposed an electron-deficiency property, conforming to the result of its zeta potential (Fig. 2**d**). Oppositely, the surface O atoms exhibited a significant electron-enrichment state after W-doping (Fig. 3**b**). Meanwhile, the charge density of Ce atom near the W atom evidently decreased, demonstrating the electron transfer from Ce atom to W atom by W–O–Ce bonds (XPS results).

The charge density differences of Ru,W co-doped CeO_2 (111) could simulate the local electronic structure of Ru-modified m-WO_x/CeO_2 interfaces (Fig. 3**c**). The substitution of Ru atom increased the partial charge density of adjacent Ce atom and W atom simultaneously, promoting the formation of low-valent Ce^{3+} and W^{5+}/W^{4+} ions. This also demonstrated more synergistic regions of $O_{V,RuCe}$ and $O_{V,m\text{-}WOx}$ at Ru-

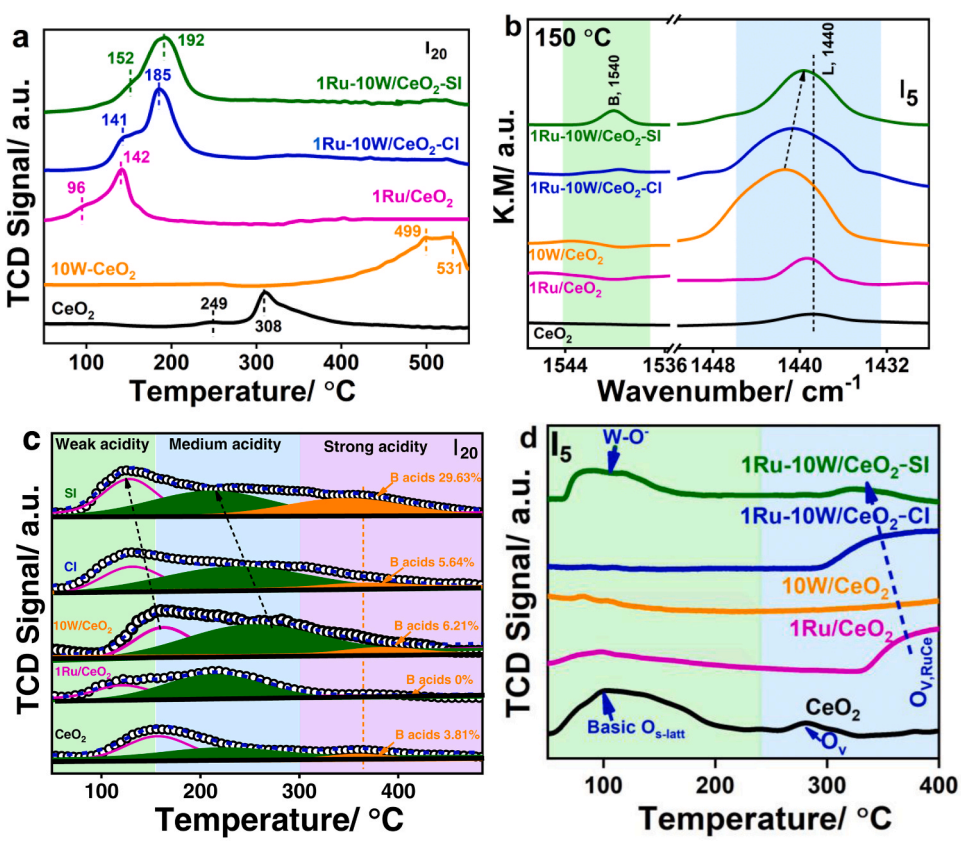

Fig. 4. (a) H_2 –TPR, (b) Py–FTIR, (c) NH_3 –TPD and (d) CO_2 –TPD of CeO_2, 1Ru/CeO_2, 10 W/CeO_2, 1Ru– 10 W/CeO_2 –CI and 1Ru– 10 W/CeO_2 –SI, respectively.

modified m-WO_x/CeO_2 interfaces. Meanwhile, the electron accumulation was still observed on the surface layer of Ru,W co-doped CeO_2 (111). The high electron density on surface layer is favorable to attract the H^+ in H_2O molecules by electrostatic interaction (nucleophyllic chemical adsorption) [45,47]. These DFT calculations were consistent with the above characterization results.

3.3. Surface redox and acid-base property

The surface redox properties of these CeO_2-based catalysts were investigated by H_2 −TPR method (Fig. 4**a**). The reduction peak of $O_{s\text{-}latt}$ for pure CeO_2 (308 ℃) evidently shifted towards a higher temperature after W modification (10 W/CeO_2, 499 ℃), indicating that the W–O–Ce decreased the reducibility and mobility of $O_{s\text{-}latt}$ of CeO_2 (XPS, PL and DFT results) [24]. On the contrary, 1Ru/CeO_2 possessed the lowest reduction peak temperatures of O_{abs} (96 ℃) and $O_{s\text{-}latt}$ (142 ℃), further demonstrating that the abundant Ru–O–Ce bonds were available for the escape of $O_{s\text{-}latt}$ to form $O_{V,RuCe}$ [25]. For the bimetal-supported CeO_2 catalysts, their reduction peaks of $O_{s\text{-}latt}$ slightly shifted towards the higher temperatures (relative to 1Ru/CeO_2), due to the negative effect of W species on redox capacity as well as the decreased Ru−O−Ce bonds (Raman, PL and DFT results). However, their reduction peak intensities were higher than that of 1Ru/CeO_2. That was because besides the reduction of Ru−O−Ce, their reduction peaks also contained the reduction of Ru−O−W (or Ru−O−W−O−Ce) linkages (120–250 ℃, Fig. S10a). And more notably, the formed Ru–O–W (or Ru−O−W−O−Ce) bonds could greatly improve the $O_{s\text{-}latt}$ mobility of m-WO_x species (Fig. S10a), and facilitated the generation of $O_{V,m\text{-}WOx}$. The H_2 −TPR profiles of 1Ru−xW/CeO_2 with the various W loadings further illustrated the differences on the distribution sites of Ru species by different impregnation methods, and the specific explanations could be seen in Fig. S10b,**c**.

To investigate the surface acidity after Ru and W loading, a pyridine (Py)−FTIR study was carried out at 150 ℃ (Fig. 4**b**). Only a weak vibration mode of Py absorbed onto L acid sites (Ce^{4+}/Ce^{3+}, 1440 cm^{-1}) was detected over pure CeO_2. Ru loading could slightly increase the peak intensity at 1440 cm^{-1}, because the modified Ru^{4+} ion with smaller radius (0.68 Å) possessed more electronegativity than Ce^{4+}/Ce^{3+} and received extra electrons [38]. 10 W/CeO_2 exhibited the highest peak intensity of L acid sites, mainly due to the large concentration of surface W^{6+} sites from m-WO_x species [24]. For 1Ru–10 W/CeO_2–CI and 1Ru–10 W/CeO_2–SI, the peak intensities of L acid sites decreased slightly (relative to 10 W/CeO_2) due to the substitution of some W^{6+} ions by Ru ions [48]. However, the peak values of Py absorbed on L acid sites produced a red-shift after Ru loading, especially for 1Ru–10 W/CeO_2–SI, indicating the decreased adsorption strength. The weakened L acid strength mainly derived from the adjustment of electronic structure of W^{6+} sites by Ru modification. According to the XPS and DFT results (Fig. 2**g** and Fig. 3), Ru modification could transform parts of W^{6+} into the lower-valent W ions (W^{5+}/W^{4+}). The W^{5+}/W^{4+} ions possessed lower electronegativity than W^{6+}, and consequently reduced the ability of receiving electrons from gas phase molecules. The L acid sites are generally favorable for the breakage of carbon bonds (such as C−Cl), however, an excess of strong L acids can impede the desorption of alkaline species (such as OH^- or Cl ions) [49]. It should be noted that 1Ru–10 W/CeO_2–SI presented the strongest peak at 1540 cm^{-1} assigned to Py absorbed on Brönsted acid sites (B acids). As known, B acids are generally associated with the W–OH sites arising from the activation-dissociation of H_2O on the unsaturated tungsten-oxygen bonds (such as W═O, O═W═O) [27]. 1Ru–10 W/CeO_2–SI possessed the abundant unsaturated tungsten-oxygen bonds (Raman results), which could provide more sites reacted with H_2O molecules. The NH_3 −TPD characterization was performed to further study the change in surface acidity, and the results were shown in Fig. 4**c**. Obviously, pure CeO_2 mainly presented the weak acid sites, and W or Ru loading could increase the integral areas of medium acids. Relative to 10 W/CeO_2, the NH_3 desorption peaks of bimetal-supported CeO_2 catalysts shifted to the lower temperatures, further indicating that the decreased L acid strength after Ru modification (Py−FTIR results). Moreover, 1Ru–10 W/CeO_2–SI exhibited an apparent NH_3 desorption peak at higher temperatures (300–400 ℃, strong acid sites). According to the analyses of Py−FTIR (Fig. 4**b**), only the 1Ru–10 W/CeO_2–SI catalyst exhibited the remarkable peak of B acids at 1540 cm^{-1}, and this was in keeping with the significant peak area of strong acid sites in NH_3 −TPD profile of 1Ru–10 W/CeO_2–SI (Fig. 4**c**). The adsorption strength of B acids to NH_3 is generally stronger than that of L acids. Meanwhile, 1Ru–10 W/CeO_2–SI had abundant unsaturated W═O bonds (or $O_{V,m\text{-}WOx}$) to generate more W−OH species according to the Raman and zeta potential results. Therefore, it could be determined that the increased strong acids in NH_3 −TPD profile of 1Ru–10 W/CeO_2–SI (Fig. 4**c**) were attributed to B acid sites. The ratios of integral areas ($A_{strong\ acids}/A_{total\ acids}$) could indirectly reflect the relative contents of B acids on catalyst surfaces. In a word, Ru modification on 10 W/CeO_2 decreased the concentration/strength of L acid sites, but promoted the formation of B acids [43].

The CO_2 −TPD measurements were performed to explore the surface alkalinity of the catalysts (Fig. 4**d**). A stronger CO_2 desorption peak at low temperatures was assigned to the surface basic lattice oxygen (weak base sites) on pure CeO_2. As known, the surface basic lattice oxygen of CeO_2 could be exchanged by Cl species during the catalytic oxidation of CVOCs [50,51]. The surface basicity of CeO_2 could be evidently decreased after Ru or W loading, especially for 10 W/CeO_2 and 1Ru− 10 W/CeO_2 −CI, and thus the exchange of chloride could become difficult. The remained low-intensity peak at 60–150 ℃ for 1Ru–10 W/CeO_2–SI could be related to the CO_2 desorption from Brönsted base sites ($W-O^-$), coming from the deprotonation of B acids at m-WO_x/CeO_2 interfaces [52,53]. Additionally, the weak peak of CeO_2 at high temperatures belonged to the CO_2 desorbed from surface O_V [50]. For Ru−W/CeO_2 catalysts, the intensities of high-temperature desorption peaks were related to the concentrations of $O_{V,RuCe}$ (H_2 −TPR and XPS results).

3.4. Catalytic performance and structure-activity relationship

The performances of DCE catalytic combustion on these Ru–W/CeO_2 catalysts were evaluated in Fig. 5 **and** Figs. S11-S13 (gas compositions: 1200 ppm DCE, 20 vol% O_2 and N_2 balance; GHSV: 30,000 mL g^{-1} h^{-1}; catalyst amount: 200 mg). Relative to 1Ru/CeO_2, all of W-modified catalysts showed better activities (Fig. 5**a**), mainly because the m-WO_x species provided more sites for DCE activation (C−Cl breakage), such as L acids (Py−FTIR results) [24]. Although 10 W/CeO_2 had the most abundant L acids (Py−FTIR results), the optimal activity was attributed to 1Ru–10 W/CeO_2–SI (Fig. 5**a**), indicating the presence of DCE activation sites that were more active than L acids on its surfaces. The T_{90} values increased in the order of 1Ru–10 W/CeO_2–SI (251.9 ℃) < 1Ru–10 W/CeO_2–CI (270.1 ℃) < 10 W/CeO_2 (272.2 ℃) < 1Ru/CeO_2 (309.5 ℃). For 1Ru/CeO_2, in spite of its high CO_2 selectivity (Fig. 5**b**), the increase of CO_x (CO_2 + CO) selectivity suddenly slowed down after 200 ℃, and unavoidable polychlorinated byproducts with the larger concentrations appeared (Fig. 5**e-i**), because of the continuous electrophilic substitution/nucleophilic addition by Cl_2 from the advantageous semi-Deacon reaction ($2Cl^-_{abs} + O_2 + O_V = Cl_2 + 2\ O_{s\text{-}latt}$) [54]. Importantly, for the bimetal-supported CeO_2 catalysts, the disappearance temperatures of VC, dichloroethylene and TCE were in advance and their extreme concentrations were significantly reduced (Fig. 5**d-f**), especially for 1Ru–10 W/CeO_2–SI. Furthermore, their polychlorinated byproducts (PCE and TeCA) could be completely inhibited (Fig. 5**h,i**), and CO_x selectivity was superior to that of 1Ru/CeO_2 after 200 ℃ (Fig. 5**b**).

Judging from the structure−activity relationship diagram (Fig. 6**a**), in addition to L acid sites, the superior activity of 1Ru–10 W/CeO_2–SI depended on the abundant B acids. The high proportion of B acid sites (NH_3 −TPD results) was accompanied with a high concentration of low-

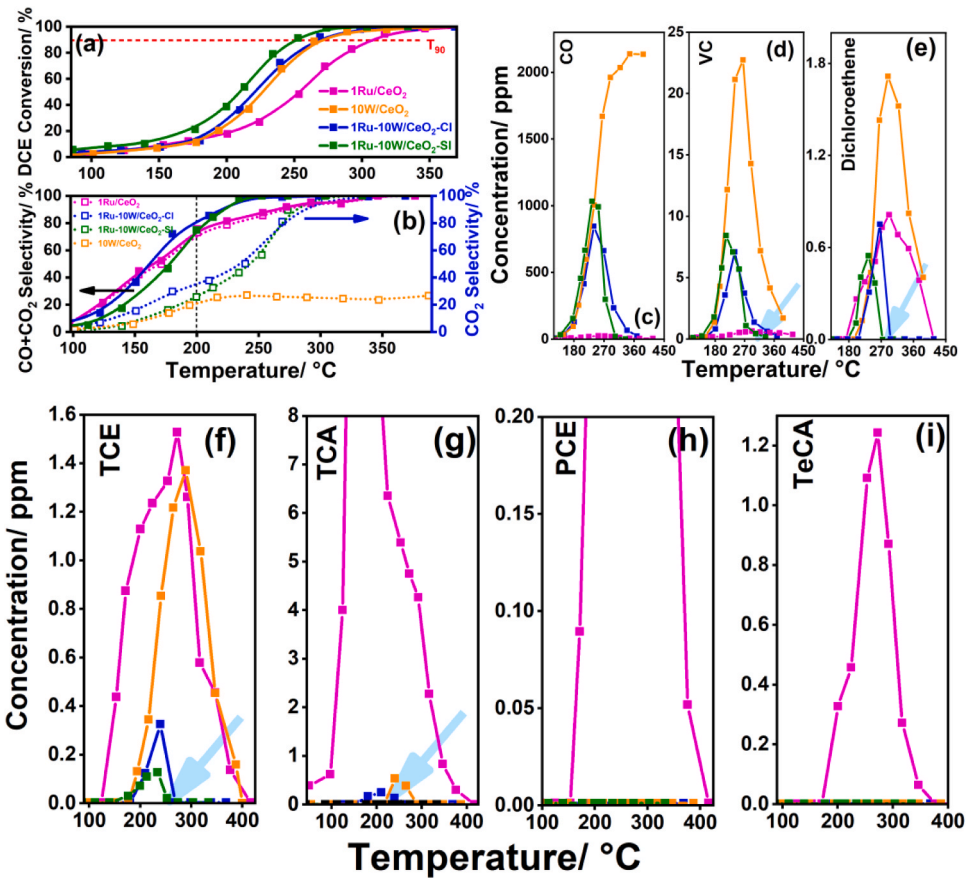

Fig. 5. (a) DCE conversion, (b) CO_2 selectivity (dotted lines) and CO_x (CO_2 + CO) selectivity (solid lines), and (c-i) temperature–concentration distributions of CO, VC, dichloroethene and polychlorinated byproducts (TCE, TCA, PCE and TeCA) for 1Ru/CeO_2, 10 W/CeO_2, 1Ru–10 W/CeO_2–CI and 1Ru–10 W/CeO_2–SI, respectively.

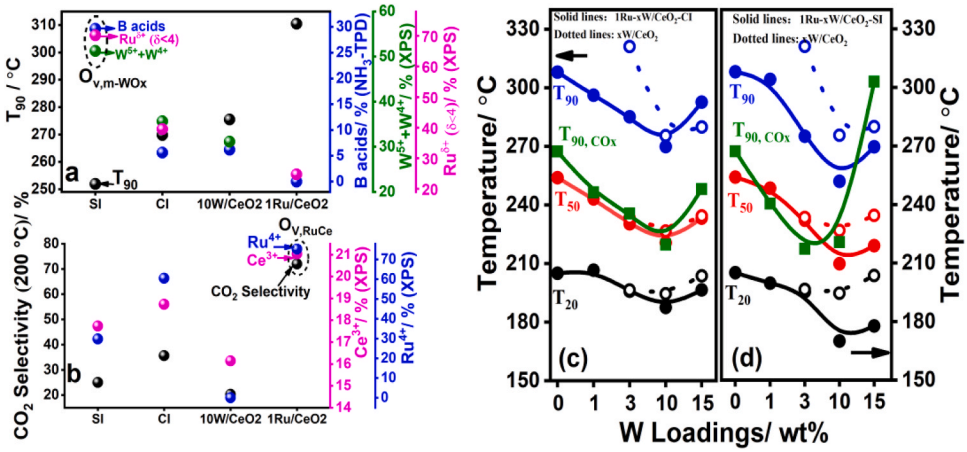

Fig. 6. . (a,b) Structure−activity relationship diagram, (c,d) T_{20}, T_{50}, T_{90} on DCE conversion, and $T_{90,COx}$ on CO_x selectivity of xW/CeO_2 (x = 3, 10, 15 wt%) and 1Ru−xW/CeO_2 −CI/SI (x = 0, 1, 3, 10, 15 wt%). $T_{90,COx}$: the temperature of CO_x selectivity reached 90%.

valent W ions (Fig. 6**a**), indicating that the formation of B acids was related to the $O_{v,m\text{-}WOx}$. The increased concentrations of $O_{V,m\text{-}WOx}$ were greatly contributed by more $Ru^{\delta+}$ ($\delta < 4$) modification at m-WO_x/CeO_2 interfaces (Fig. 6**a**). For 1Ru–10 W/CeO_2–CI, given most Ru species doped into the CeO_2 surfaces rather than m-WO_x, the increase in activity was not significant relative to 10 W/CeO_2 (Fig. 5**a**). The 1Ru/CeO_2 exhibited the optimal CO_2 selectivity while the CO_2 selectivity of 10 W/CeO_2 only reached 20% along with the highest CO concentration (Fig. 5**b,c**). According to the structure−activity relationship diagram (Fig. 6**b**), it could be asserted that CO_2 selectivity depended on the concentration of $O_{v,RuCe}$. The more $O_{v,RuCe}$ represented the better mobility of $O_{s\text{-}latt}$ from Ru−O−Ce linkages, facilitating the deep oxidation of intermediate products. The extremely low CO_2 selectivity of 10 W/CeO_2 was attributed to the negative effects of W−O−Ce on the $O_{s\text{-}latt}$ mobility of CeO_2 (DFT, XPS, PL and H_2 −TPR results). The higher extreme concentration of VC for 10 W/CeO_2 (Fig. 5**d**) stemmed from the facile dehydrochlorination owing to its abundant L acids but negligible redox property (Py−FTIR and H_2 −TPR results).

The CO_2 selectivity of 1Ru/CeO_2 during the stability test exhibited a significant volatility (Fig. S14a), and this was mainly related to the adsorption−desorption process of surface Cl species at T_{90} [25]. The obvious Cl 2p XPS signal of the used 1Ru/CeO_2 (Fig. S14c) demonstrated the inevitable Cl adsorption on its surfaces. The markedly rising Cl_2 signal after 400 ℃ in TPO profile of the used 1Ru/CeO_2 stemmed from the surface Deacon reaction (Fig. S15). Therefore, it is worth noting that the good Deacon reactivity of 1Ru/CeO_2 catalysts does not completely eliminate the Cl absorption [11–13], especially in long-term operation. The addition of W could stabilize the CO_2 curves, especially for 1Ru− 10 W/CeO_2 −SI catalyst (Fig. S14b), because more B acid sites made the Cl species quickly leave the surfaces in the form of HCl. A rising CO_2 signal of the used 10 W/CeO_2 at high temperatures was related to the accumulation of coking species on surfaces (Fig. S15) due to its poor redox property and strong L acidity [24,52]. However, too strong L acidity on 10 W/CeO_2 also inevitably leaded to the occupation of Cl species to form surface metal chloride oxides (WO_2Cl_2), resulting in the further chlorination (higher concentrations of dichloroethene and TCE, Fig. 5**e,f**) [24,26]. The weakly increased Cl_2/HCl signals in TPO profiles of the used 10 W/CeO_2 after 450 ℃ further demonstrated the existence of surface WO_2Cl_2 species (Fig. S15). The Cl 2p XPS peaks were almost undetectable on 1Ru-10 W/CeO_2-CI and 1Ru-10 W/CeO_2-SI catalysts (Fig. S14c). Meanwhile, for the used 1Ru/CeO_2, the surface relative concentration of Ce^{3+} evidently decreased and the Ce^{4+} 3d XPS peak value shifted to a higher binding energy as compared to the fresh one (Fig. S14d **and** Fig. 2**f**), because the Cl species occupied the surface oxygen vacancies. However, 1Ru− 10 W/CeO_2 −CI and 1Ru− 10 W/-CeO_2 −SI catalysts showed the opposite, because part of Ce^{4+} could be reduced by hydrocarbon species under the condition of less Cl adsorption during the catalytic oxidation [8]. There were almost no evident CO_2/Cl_2/HCl signals in TPO profiles of the bimetal-supported CeO_2 catalysts after stability tests (Fig. S15). These good phenomena originated from the synergistic effects between $O_{V,RuCe}$ and $O_{V,m\text{-}WOx}$. But a small amount of TCA could still be detected over 1Ru–10 W/CeO_2–CI (Fig. 5**g**), indicating that the semi-Deacon reaction still occurred at $O_{V,RuCe}$ far away from m-WO_x/CeO_2 interfaces. Compared with the recently reported results obtained on Ce-based catalysts and other metal oxide catalysts, 1Ru–10 W/CeO_2–SI catalyst presents the increased activity (low T_{50} and T_{90}) for DCE oxidation (Table S2), which further demonstrated the advantage of synergistic effects between $O_{V,RuCe}$ and $O_{V,m\text{-}WOx}$ on 1Ru–10 W/CeO_2–SI surfaces.

The effects of various W loadings on the catalytic performances of xW/CeO_2 and 1Ru–xW/CeO_2 were exhibited in Fig. 6**b** and Figs. S11-S13. For xW/CeO_2, DCE conversions exhibited a trend of increasing first and subsequently decreasing with the increase in W loadings (Fig. S11a), and 10 wt% W presented the excellent activity due to the monolayer dispersion of WO_x species (m-WO_x) on CeO_2 surfaces (characterization results). Wang et al. also proved that the m-WO_x/CeO_2 interfaces could provide more highly-unsaturated W^{6+} (strong L acid sites) and W–OH sites (B acid sites) to promote the chlorobenzene degradation [24]. The tendency of activity as a function of W content over the bimetal-supported CeO_2 catalysts was consistent with that of xW/CeO_2 (Figs. S12 and S13), indicating that Ru addition could not change the dispersion form of m-WO_x (STEM results), either by CI or SI impregnation. Meanwhile, the lower extreme concentrations and earlier disappearing temperatures of dichloroethene and polychlorinated byproducts at the W loading of 10 wt% (Fig. S12c**,d and** Fig. S13c**,d**), further demonstrated that only the m-WO_x could form a advantageously synergistic effects with the Ru−O−Ce linkages. The increase in activity (T_{20}, T_{50}, T_{90}) of 1Ru−xW/CeO_2 −SI (relative to xW/CeO_2) was more obvious than that of 1Ru−xW/CeO_2 −CI under the same W content, because SI impregnation was more conducive to the B acid sites (or $O_{V,m\text{-}WOx}$) formed. Although the CO_2 selectivity of 1Ru−xW/CeO_2 ($x < 15$) exhibited a gradual decrease with the increased W contents (H_2 −TPR results in Fig. S10b**,c**), their CO_x selectivity was always higher that of 1Ru/CeO_2 after 200 ℃ ($T_{90,COx}$, Fig. 6**b**, Fig. S12a **and** Fig. S13a), which further illustrated the existence of synergistic effects between $O_{V,RuCe}$ and $O_{V,m\text{-}WOx}$.

3.5. Reaction mechanism

According to the TPSR profiles (Fig. S16) and in situ FTIR spectra of DCE adsorption/oxidation on 1Ru/CeO_2 (Fig. 7**a** and Fig. S17a) and 10 W/CeO_2 (Fig. 7**b** and Fig. S17b), some important conclusions were drawn as follows. The adsorption/activation sites of DCE on 1Ru/CeO_2 surfaces were mainly assigned to the $O_{V,RuCe}$ rather than surface hydroxyl groups (Ce−OH) [37,55,56]. The DCE degradation on 1Ru/CeO_2 followed MvK mechanism, and the excellent mobility of $O_{s\text{-}latt}$ from Ru−O−Ce linkages was the key factor for rapid oxydehydrogenation and deep oxidation of intermediate products. However, the Cl species adsorbed on $O_{V,RuCe}$ were easily oxidized by semi-Deacon reaction and generated more Cl_2 after 350 ℃ (TPSR results, Fig. S16). For 10 W/CeO_2, strong L acids and W−OH were the main active sites for DCE adsorption/activation [25,55,58–60]. The supplement of hydroxyl groups (W−OH) came from the activation/dissociation of H_2O on W═O sites ($O_{V,m\text{-}WOx}$) at m-WO_x/CeO_2 interfaces. The DCE degradation on 10 W/CeO_2 mainly followed the L−H mechanism [24]. The detailed analyses and explanations were presented in the section of "**Reaction mechanism**" of Supporting Information (Fig. S17 and Scheme S1).

For 1Ru− 10 W/CeO_2 −CI catalyst, various alcohols could be detected in the in situ FTIR spectra of DCE adsorption at low temperatures (50–200 ℃, Fig. 7**c**), such as enolic species (CH_2 =CHOH, 1443 cm^{-1}), chloroethanol ($ClCH_2CH_2OH$, 1238 and 1165 cm^{-1}) and other alcohols absorbed on L acid sites (1110–1260 cm^{-1}) [58,60]. These alcohols derived from the substitution of Cl on DCE/VC by W−OH at m-WO_x/CeO_2 interfaces. Meanwhile, the characteristic bands of carbonates (ν (CO_3^{2-}), 1537 and 1490 cm^{-1}) could be detected at low temperatures (before 250 ℃, Fig. 7**c**). Importantly, relative to 10 W/CeO_2 (Fig. 7**b**), the accumulation of incomplete oxidation products was barely noticeable under O_2 free conditions at higher temperatures (Fig. 7**c**). All of these phenomena indicated that the $O_{s\text{-}latt}$ from Ru−O−Ce was the critical active sites for the oxygenolysis of intermediate products formed at m-WO_x/CeO_2 interfaces. Under aerobic conditions (Fig. S17c), the characteristic bands at 1233, 1286, 1312 and 1429 cm^{-1} were attributed to the δ (C−H) of DCE adsorbed on L acid sites at low temperatures (50–100 ℃) [55]. In addition, the evidently negative bands of W−OH (3604 cm^{-1}) and rapidly disappearing carbonates (Fig. S17c) further demonstrated the synergistic effects between acid sites at m-WO_x/CeO_2 interfaces and $O_{s\text{-}latt}$ from Ru−O−Ce bonds for DCE activation−oxidation. Relative to 10 W/CeO_2, 1Ru− 10 W/CeO_2 −CI exhibited the lower Cl_2 concentration at high temperatures (Fig. S16) mainly due to the decreased adsorption strength of Cl species on L acids (electronic effects, NH_3 −TPD, Py−FTIR and DFT results).

Interestingly, for 1Ru− 10 W/CeO_2 −SI, the band at 3255 cm^{-1} of hydrogen-bonded water (W−OH···H_2O) was the most prominent before 300 ℃ in the in situ FTIR spectra of DCE adsorption (Fig. 7**d**), which also indicated the abundant W−OH with the highly reactive H^+ on its surfaces [25,53,60]. This active W−OH could rapidly perform the activation/dechloridation of DCE and VC. The characteristic bands of DCE absorbed on L acids were nearly undetectable at 50–100 ℃ (Fig. 7**d** and Fig. S17d), further indicting that DCE could be rapidly activated/dechlorinated on active W–OH rather than L acid sites. The obvious bands at 2330 cm^{-1} (Fig. S18d) assigned to the CO_2 adsorbed on Brönsted base sites (W−O^-), further indicating the facile deprotonation of ample W−OH on 1Ru− 10 W/CeO_2 −SI surfaces (CO_2 −TPD results). On the one hand, 1Ru− 10 W/CeO_2 −SI possessed the abundant highly-unsaturated O═W═O bonds due to more Ru species interacted with m-WO_x, which could accept more H_2O to form more active W−OH (Py−FTIR and NH_3 −TPD results). On the other hand, Ru modification (Ru–O–W or Ru–O–W–O–Ce bonds) further improved the mobility of $O_{s\text{-}latt}$ at m-WO_x/CeO_2 interfaces (H_2 −TPR results). The activated $O_{s\text{-}latt}$ at m-WO_x/CeO_2 interfaces also made a great contribution to the rapid

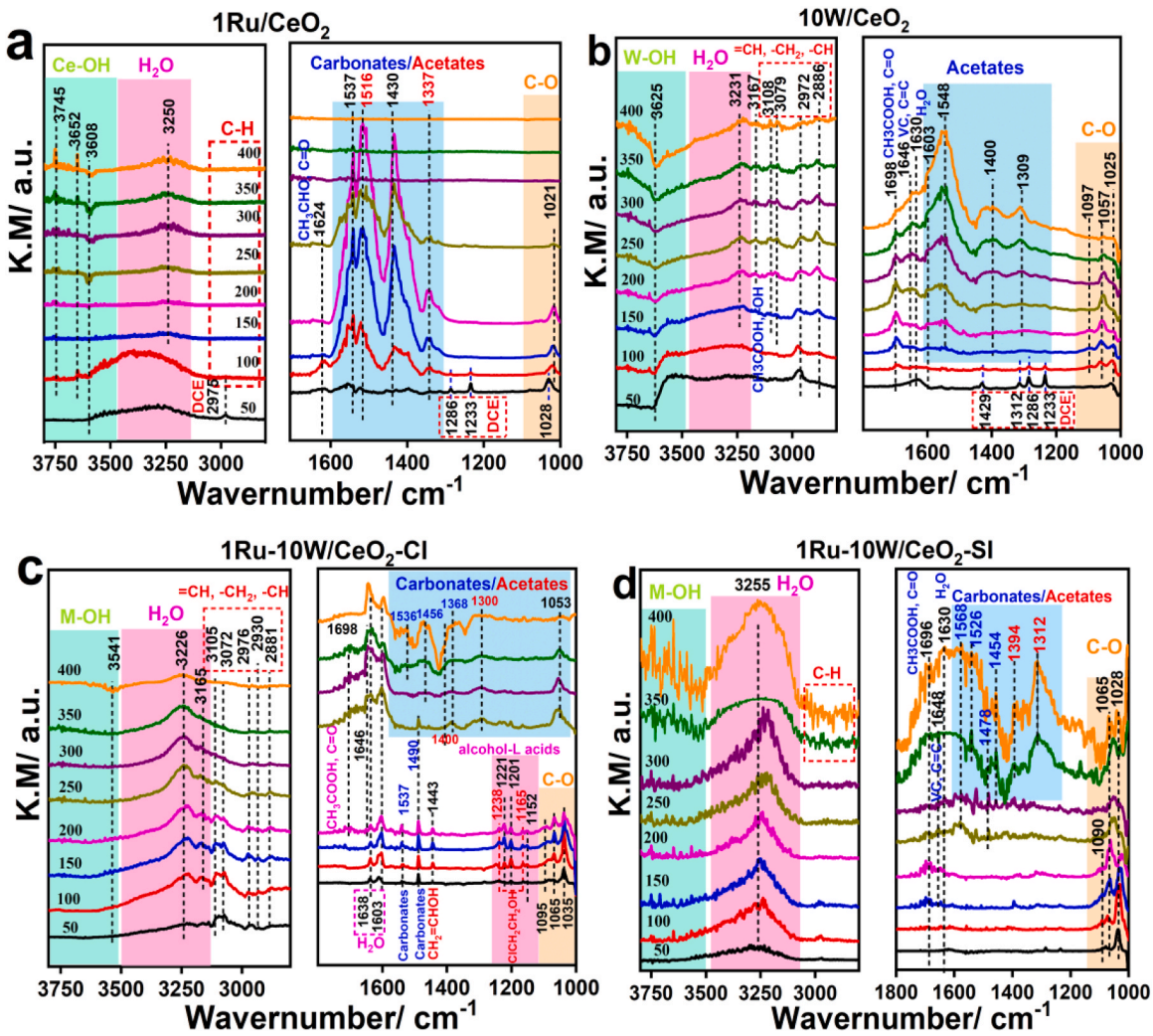

Fig. 7. *In situ* FTIR spectra of DCE adsorption on (a) 1Ru/CeO_2, (b) 10 W/CeO_2, (c) 1Ru− 10 W/CeO_2 −CI, (d) 1Ru− 10 W/CeO_2 −SI catalysts, respectively.

oxydehydrogenation of DCE and intermediate products before 300 ℃. This was also the reason why the characteristic bands of C–H bonds were almost undetectable at low temperatures (Fig. 7**d**). The consumption of $O_{s\text{-latt}}$ at m-WO_x/CeO_2 interfaces could leave more $O_{V,m\text{-}WOx}$, which could be transformed into more O═W═O bonds for continuous H_2O adsorption/dissociation under O_2 free conditions (Scheme 1). Nevertheless, when the rate of H_2O adsorption/dissociation on $O_{V,m\text{-}WOx}$ was much faster than that of hydroxyl depletion at high temperatures (after 300 ℃, Fig. 7**d**), it would result in a serious accumulation of H_2O. The appearance of many remarkably positive bands assigned to the free O−H bonds (3500–3750 cm^{-1}, Fig. 7**d**) after 300 ℃ further demonstrated the above opinion [25,60]. Unfortunately, without the sufficiently activated $O_{s\text{-latt}}$ from Ru–O–Ce bonds for further deep oxidation, the accumulation of carbonates/acetates appeared after 300 ℃ (Fig. 7**d**). After O_2 introduced, the accumulation of absorbed H_2O slightly decreased at high temperatures (Fig. S17d), which was associated with the competitive adsorption between O_2 and H_2O on $O_{V,m\text{-}WOx}$. This also strongly demonstrated that the $O_{V,m\text{-}WOx}$ was more propitious to the adsorption/activation of H_2O (relative to O_2), which provided a large number of active H^+ and made the Cl species quickly leave the surfaces in the form of HCl (TPSR results, Fig. S16). The main adsorbed species were carbonates rather than acetates (Fig. S17d), further indicating that the oxydehydrogenation of intermediate products was accelerated in the presence of O_2. And the accumulated carbonates/acetates were also attenuated under O_2 conditions at 300–400 ℃ (Fig. S17d), due to the favorable exchange between O_2 and $O_{s\text{-latt}}$ from Ru−O−Ce. Therefore, the enhanced synergistic effects on 1Ru− 10 W/CeO_2 −SI relied on the rapid dechlorination and fast oxydehydrogenation at Ru-modified m-WO_x/CeO_2 interfaces. The differences in the possible reaction paths of 1Ru− 10 W/CeO_2 −SI and 1Ru− 10 W/CeO_2 −CI were displayed in Scheme 1.

3.6. *Effects of H_2O*

In general, the concentrations of CVOCs in the exhaust gases are not more than 1000 mg m^{-3}, and the water vapor is the main component affecting the performance of the catalysts. The specific effects of water vapor on these CeO_2-based catalysts were displayed in Fig. 8 **and** Figs. S19-S21. For 1Ru/CeO_2 (Fig. 8**a**), both DCE conversion and CO_2 selectivity decreased after H_2O added due to the competitive adsorption of H_2O and O_2 on $O_{V,RuCe}$ [57]. For the W-loaded catalysts, the decreased activities (especially for 10 W/CeO_2) were mainly related to the occupation of L acids (important active sites for C−Cl breakage) by H_2O (Fig. 8**a**) [24]. The detailed effects of H_2O on 1Ru/CeO_2 and 10 W/CeO_2 were presented in the section of "**Effects of H_2O**" of **Supporting Information**.

However, relative to 10 W/CeO_2 (Fig. S19b), the band of absorbed H_2O (3247 cm^{-1}) seemed very weak over 1Ru–10 W/CeO_2 −CI (Fig. S19c), primarily because the co-loaded Ru could weaken the ability of L acid sites to accept electrons (DFT, NH_3 −TPD and Py−FTIR results) and decrease the absorption strength of H_2O at m-WO_x/CeO_2 interfaces. The facile desorption of H_2O from m-WO_x/CeO_2 interfaces could take

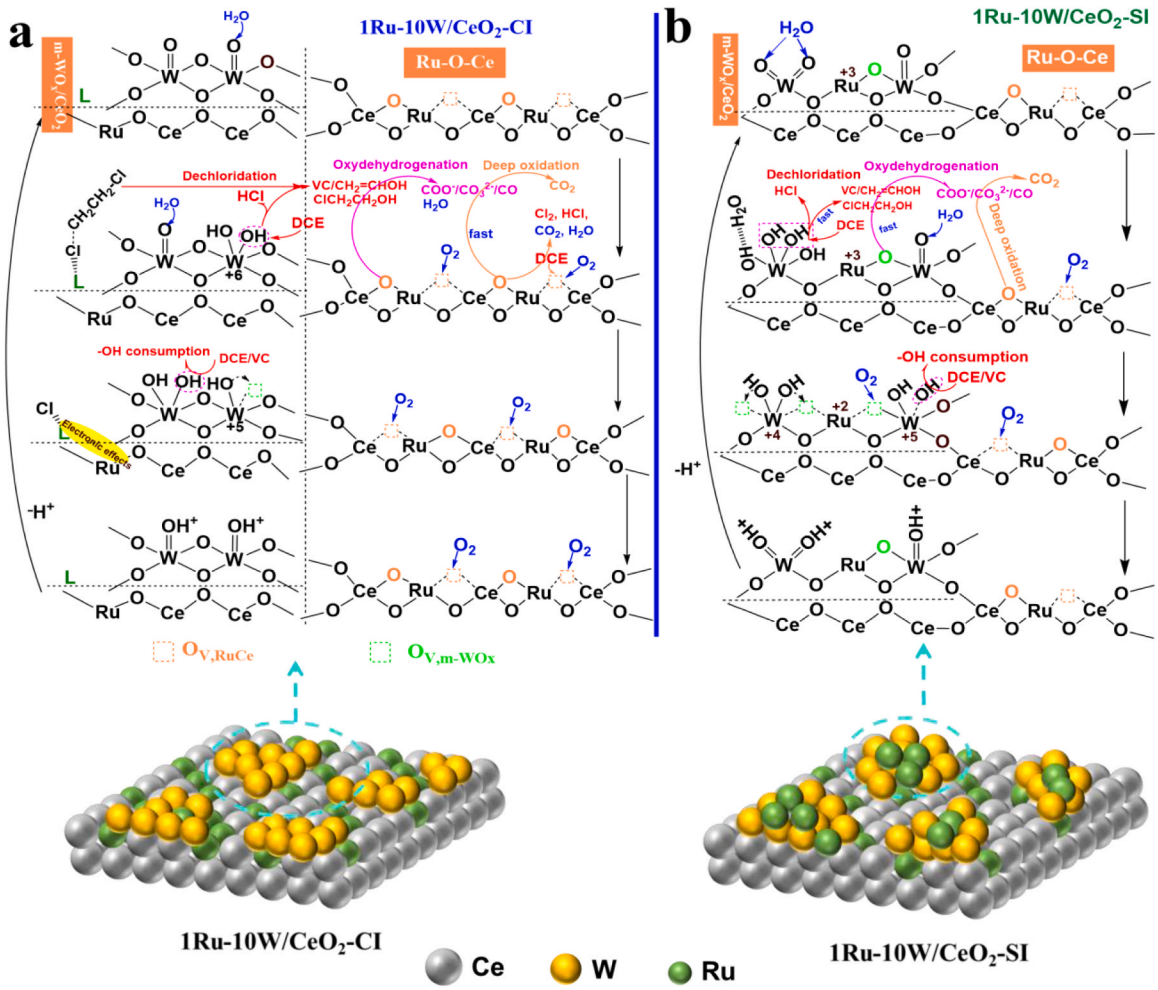

Scheme 1. The possible reaction paths and distributions of active sites for (a) 1Ru− 10 W/CeO_2 −CI and (b) 1Ru− 10 W/CeO_2 −SI.

away the Cl species adsorbed on $O_{V,RuCe}$ (cleaning effects, Scheme S2a), inhibiting the Deacon reaction and promoting the exchange of O_2 and $O_{s\text{-}latt}$ at m-WO_x/CeO_2 interfaces. The CO_2 selectivity increased (Fig. 8**b**), CO concentration significantly decreased (Fig. S20a) and TCA disappeared (Fig. S20e **and** Fig. S21e) over 1Ru− 10 W/CeO_2 −CI in wet conditions reflected the above view.

As compared to 10 W/CeO_2 (Fig. 8**c**), the DCE conversion of 1Ru− 10 W/CeO_2 −CI decline more slowly over time at "H_2O off", mainly due to the reduced absorption strength of Cl species on L acids (electronic effects). In addition, its CO_2 selectivity decreased (Fig. 8**d**) but CO concentration increased over time at "H_2O off" (Fig. S21a). This was related to the inevitable adsorption of Cl species at $O_{V,RuCe}$ far away from m-WO_x/CeO_2 interfaces during a long-running test (Fig. S15 and Fig. S16). But the CO_2 selectivity at "H_2O on" showed an increasing trend over time (Fig. 8**d**), further indicating the timely cleaning effects of weakly adsorbed H_2O for $O_{V,RuCe}$ (Scheme S2a).

For 1Ru− 10 W/CeO_2 −SI, the band of absorbed H_2O at m-WO_x/CeO_2 interfaces exhibited a decreasing trend firstly (100–200 ℃, Fig. S19d) with the increased CO_2 selectivity (Fig. 8**b**) due to the same electronic effect as 1Ru− 10 W/CeO_2 −CI above (DFT, NH_3 −TPD and Py−FTIR results). Subsequently, the band of absorbed H_2O obviously enhanced after 200 ℃ (Fig. S19d). The main reason was that the rapid escape of $O_{s\text{-}latt}$ at Ru-modified m-WO_x/CeO_2 interfaces could leave more $O_{V,m\text{-}WOx}$ to adsorb/dissociate H_2O (Fig. 7**d and** Scheme 1**b**), causing lots of active W−OH (3750–3500 cm^{-1}). The active W−OH could attract water molecules by electrostatic interaction to form hydrogen-bonded water (W−OH···H_2O, 3268 cm^{-1}, Fig. S19d) in wet conditions [53]. Afterwards, the excessive W−OH···H_2O could overflow to the closer $O_{V,RuCe}$, preventing the exchange of O_2 and $O_{s\text{-}latt}$ (Scheme S2b). The lowered CO_2 selectivity (Fig. 8**d**) and increased disappearance temperature of CO (Fig. S20a) over 1Ru–10 W/CeO_2–SI after 200 ℃ demonstrated this view.

For 1Ru–10 W/CeO_2–SI, there was a slight increase in DCE conversion over time at "H_2O on" because the extra H_2O provided a rich source of active W–OH for DCE activation (Fig. 8**d**). However, the CO_2 selectivity gradually decreased and CO concentration increased over time, either at "H_2O off" or "H_2O on" after 6 h (Fig. 8**d** and Fig. S21a), which could be assigned to the accumulated W−OH···H_2O at Ru-modified m-WO_x/CeO_2 interfaces during the long-term tests (spillover effects, Scheme S2b). Importantly, all chlorinated by-products (except for VC) could be completely inhibited in wet conditions for both 1Ru–10 W/CeO_2–CI and 1Ru–10 W/CeO_2–SI (Fig. S20c**-g and** Fig. S21c**-g**) due to the synergistic effects.

4. Conclusions

In this study, the effects of different impregnation methods (CI and SI) of Ru/W–CeO_2 catalysts on DCE catalytic oxidation were studied. Whether for SI or CI, the monolayer dispersed WO_x species (m-WO_x, 10 wt% W) on CeO_2 surfaces always contributed the better activities. There were two main types of oxygen vacancies ($O_{V,RuCe}$ and $O_{V,m\text{-}WOx}$) respectively located at Ru−O−Ce bonds and m-WO_x/CeO_2 interfaces. The $O_{V,m\text{-}WOx}$ determined the DCE activation while the deep oxidation of intermediate products relied on the $O_{V,RuCe}$. The amounts of $O_{V,m\text{-}WOx}$

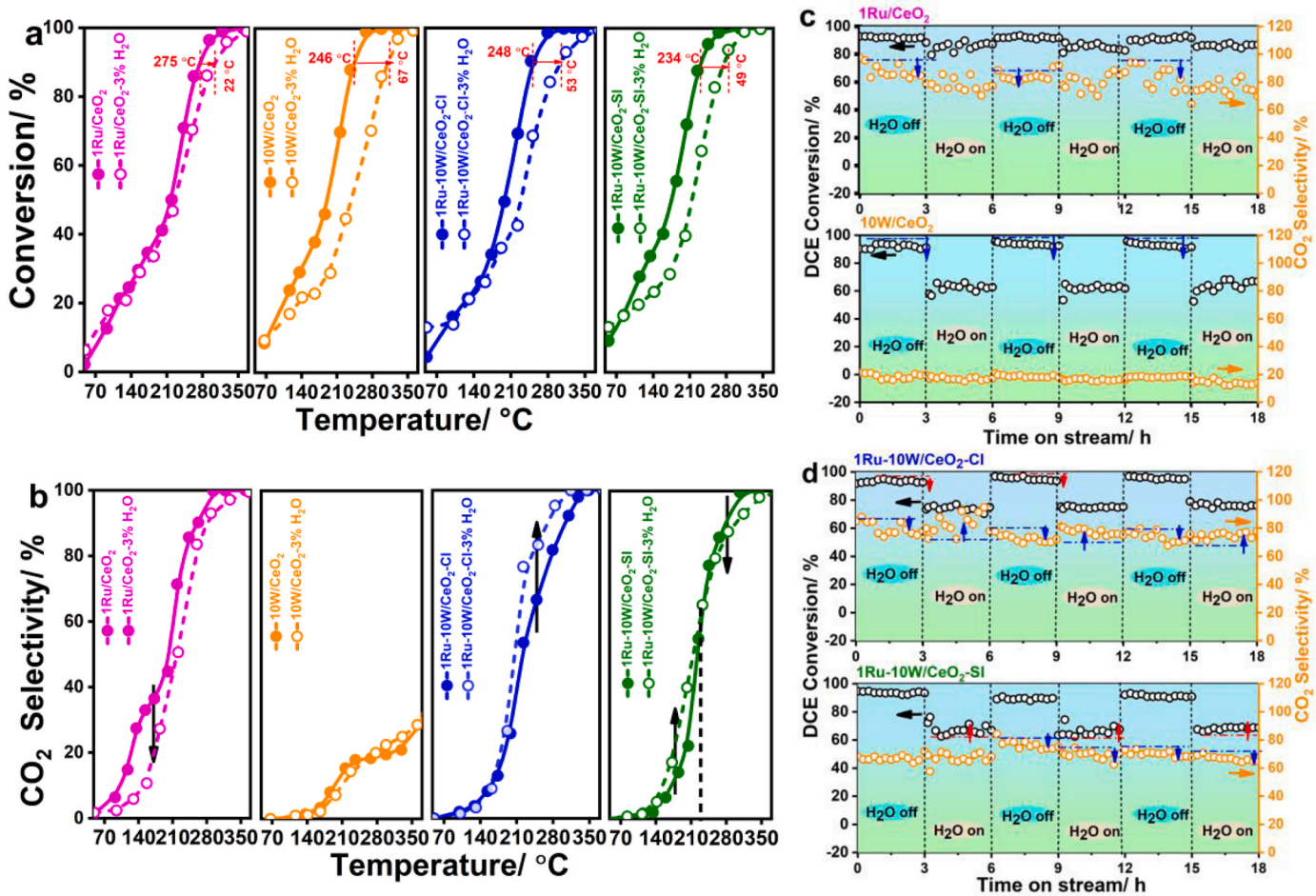

Fig. 8. Effects of 3 vol% water vapor on (a) DCE conversion and (b) CO_2 selectivity, and (c) DCE conversion and (d) CO_2 selectivity as a function of time-on-stream at T_{90} over various catalysts. Reaction conditions: 1000 mg m^{-3} DCE + 3 vol% H_2O + 20 vol% O_2 (N_2 as balance gas).

and $O_{V,RuCe}$, and the synergetic degree between them depended on the distribution states of active sites. For 1Ru–10 W/CeO_2-SI, more Ru species were distributed on m-WO_x. The Ru modification could further increase the mobility of $O_{s\text{-}latt}$ at m-WO_x/CeO_2 interfaces by Ru–O–W (or Ru–O–W–O–Ce), accelerating the oxydehydrogenation of intermediate products. Meanwhile, the escape of $O_{s\text{-}latt}$ at m-WO_x/CeO_2 interfaces left more $O_{V,m\text{-}WOx}$, promoting the formation more highly-unsaturated O═W═O bonds and active W–OH (B acid sites), and accelerating the dechlorination of DCE/VC. For 1Ru–10 W/CeO_2–SI, the closer contact between Ru−O−Ce and m-WO_x/CeO_2 interfaces provided a stronger synergy effect, resulting in the higher activity/CO_x selectivity and inhibited the Cl poisoning/Cl_2/polychlorinated byproducts. But too many active W–OH easily caused the accumulated W−OH···H_2O at m-WO_x/CeO_2 interfaces in wet conditions. Oppositely, for 1Ru–10 W/CeO_2–CI, the main landing sites of Ru species were CeO_2 surfaces rather than m-WO_x species. The weak semi-Deacon reaction still occurred on $O_{V,RuCe}$ far away from m-WO_x/CeO_2 interfaces. However, 1Ru–10 W/CeO_2–CI could weaken the adsorption strength of L acid sites to H_2O/Cl species due to the electronic effects. The desorption of H_2O at m-WO_x/CeO_2 interfaces facilitated the timely cleaning of Cl species on $O_{V,RuCe}$.

CRediT authorship contribution statement

Yao Shuiliang: Resources, Writing – review & editing. **Shi Yuliang:** Formal analysis, Visualization. **Wu Zuliang:** Data curation, Visualization. **Gao Erhao:** Data curation, Visualization. **Li Jing:** Data curation, Visualization. **Dai Qiguang:** Funding acquisition, Writing – review & editing, Resources. **Meng Xinyu:** Conceptualization, Data curation, Formal analysis, Writing – original draft, Investigation, Validation. **Zhu Jiali:** Investigation, Visualization. **Wang Wei:** Funding acquisition, Project administration, Resources, Supervision, Writing – review & editing. **Wang Qirui:** Conceptualization, Methodology, Writing – review & editing. **Sun Yan:** Investigation, Supervision. **Zhang Tiantian:** Conceptualization, Methodology.

Declaration of Competing Interest

The authors declare that they have no known competing financial interests or personal relationships that could have appeared to influence the work reported in this paper.

Data availability

Data will be made available on request.

Acknowledgements

This work was financially supported by National Natural Science Foundation of China (Grant No. 22106010), Postgraduate Research Innovation Program of Jiangsu Province [KYCX22_3111], and Introduction and Cultivation of Leading Innovative Talents Foundation of Changzhou, Jiangsu Province (grant CQ20210108).

Appendix A. Supporting information

Supplementary data associated with this article can be found in the

online version at doi:10.1016/j.apcatb.2023.123664.

References

[1] C.L. Li, Y.X. Zhao, H. Song, H. Li, A review on recent advances in catalytic combustion of chlorinated volatile organic compounds, J. Chem. Technol. Biot. 95 (2020) 2069–2082.

[2] Y. Su, K.X. Fu, C.H. Pang, Y.F. Zheng, C.F. Song, N. Ji, D.G. Ma, X.B. Lu, C.X. Liu, R. Han, Q.L. Liu, Recent advances of chlorinated volatile organic compounds' oxidation catalyzed by multiple catalysts: reasonable adjustment of acidity and redox properties, Environ. Sci. Technol. 56 (2022) 9854–9871.

[3] Q.Y. Wang, K.L. Yeung, M.A. Bañares, Ceria and its related materials for VOC catalytic combustion: a review, Catal. Today 356 (2020) 141–154.

[4] H.Q. Jia, Y. Xing, L.G. Zhang, W.B. Zhang, J.Q. Wang, H. Zhang, W. Su, Progress of catalytic oxidation of typical chlorined volatile organic compounds (CVOCs): A review, Sci. Total. Environ. 865 (2023), 161063.

[5] W. Wang, Q. Zhu, Q.G. Dai, X.Y. Wang, Fe doped CeO_2 nanosheets for catalytic oxidation of 1,2-dichloroethane: Effect of preparation method, Chem. Eng. J. 307 (2017) 1037–1046.

[6] K. Shen, M.X. Jiang, X.W. Yang, W.Z. Zhou, Q.G. Dai, X.Y. Wang, L. Wang, Y. Guo, Y.L. Guo, W.C. Zhan, Low-temperature catalytic combustion of trichloroethylene over MnO_x-CeO_2 mixed oxide catalysts, J. Rare. Earth. 41 (2023) 523–530.

[7] C. Wang, C.H. Zhang, W.C. Hua, Y.L. Guo, G.Z. Lu, S. Gil, A.G. Fendler, Catalytic oxidation of vinyl chloride emissions over Co-Ce composite oxide catalysts, Chem. Eng. J. 315 (2017) 392–402.

[8] K. Shen, B. Gao, H.Q. Xia, W. Deng, J.R. Yan, X.H. Guo, X.Y. Wang, W.C. Zhan, Q. G. Dai, Oxy-anionic doping: a new strategy for improving selectivity of Ru/CeO_2 with synergetic versatility and thermal stability for catalytic oxidation of chlorinated volatile organic compounds, Environ. Sci. Technol. 56 (2022) 8854–8863.

[9] J. Chen, C.Q. Wang, X.L. Lv, G.X. Huang, W.J. Xu, X.L. Li, H.P. Jia, Pt/CeO_2 coated with polyoxometallate chainmail to regulate oxidation of chlorobenzene without hazardous by-products, J. Hazard. Mater. 441 (2023), 129925.

[10] B.Y. Guo, X.Y. Niu, J.J. Yang, L. Li, Q.Y. Chen, J. Zhou, Ultra-fast catalytic hydrodechlorination of chloroacetic acids over Pd catalyst supported on CeO_2 with exposed (110) plane, Chem. Eng. J. 472 (2023), 145126.

[11] Y.P. Liu, S.Y. Li, X.Q. Lu, R. Ma, Y.H. Fu, S.H. Wang, L.Y. Zhou, W.D. Zhu, Insights into the Sintering Resistance of RuO_2/TiO_2-SiO_2 in the Deacon Process: Role of SiO_2, Catal. Sci. Technol. 11 (2021) 5460–5466.

[12] Q.G. Dai, S.X. Bai, X.Y. Wang, G.Z. Lu, Catalytic combustion of chlorobenzene over Ru-doped ceria catalysts: mechanism study, Appl. Catal. B 129 (2013) 580–588.

[13] Z. Zheng, Y. Yang, H. Li, Q. Xin, S. Zhang, Y. Liu, S.J. Liu, C.H. Zheng, H. Song, X. Gao, Effect of multi-pollutant on the catalytic oxidation of dichloromethane over RuO_2-WO_3/$Sn_{0.2}Ti_{0.8}O_2$ catalyst, Fuel 278 (2020), 118207.

[14] Q.G. Dai, L.L. Yin, S.X. Bai, W. Wang, X.Y. Wang, X.Q. Gong, G.Z. Lu, Catalytic total oxidation of 1, 2-dichloroethane over VO_x/CeO_2 catalysts: Further insights via isotopic tracer techniques, Appl. Catal. B 182 (2016) 598–610.

[15] H. Zhang, X.H. Gao, B.W. Gong, S.J. Shao, C.S. Tu, J. Pan, Y.Y. Wang, Q.G. Dai, Y. L. Guo, X.Y. Wang, Catalytic combustion of CVOCs over MoO_x/CeO_2 catalysts, Appl. Catal. B 310 (2022), 121240.

[16] B.D. Rivas, C. Sampedro, E.V. Ramos-Fernández, R. López-Fonseca, J. Gascon, M. Makkee, J.I. Gutiérrez-Ortiz, Influence of the synthesis route on the catalytic oxidation of 1, 2-dichloroethane over CeO_2/H-ZSM5 catalysts, Appl. Catal. A 456 (2013) 96–104.

[17] J.W. Chen, Q.J. Meng, F. Bi, J.K. Chen, X.L. Weng, Z.B. Wu, Characteristics of catalytic destruction of dichloromethane and ethyl acetate mixture over H_xPO_4–RuO_x/CeO_2 catalyst, J. Environ. Sci. (2023).

[18] S. Yang, Y.F. Chen, H.W. Guo, X.Z. Jiang, J.W. Ma, X.Y. Li, Z. Chen, X.D. Ma, Oxygen vacancies enriched Nb-WO_x supported Ru for polychlorinated aromatics oxidation: Reaction mechanism exploration, Fuel 324 (2022), 124501.

[19] Q.G. Dai, K. Shen, W. Deng, Dai, Y.P. Cai, J.R. Yan, J.Y. Wu, L.M. Guo, R. Liu, X. Y. Wang, W.C. Zhan, HCl–Tolerant H_xPO_4/RuO_x–CeO_2 Catalysts for Extremely Efficient Catalytic Elimination of Chlorinated VOCs, Environ. Sci. Technol. 55 (2021) 4007–4016.

[20] Y.P. Long, Q.J. Meng, M.L. Chen, X.Q. Luo, Q.G. Dai, H.F. Lu, Z.B. Wu, X.L. Weng, Selective Ru Adsorption on SnO_2/CeO_2 Mixed Oxides for Efficient Destruction of Multicomponent Volatile Organic Compounds: From Laboratory to Practical Possibility, Environ. Sci. Technol. 56 (2022) 9762–9772.

[21] N. Guo, J.Y. Zhang, L.X. Jiang, D.T. Wang, Z.W. Wang, Highly efficient and selective Ru and Ce modified ZSM-5 catalysts for catalytic oxidation of toluene, Colloid Surf. A 651 (2022), 129709.

[22] W. Wang, Q. Zhu, F. Qin, Q.G. Dai, X.Y. Wang, Fe doped CeO_2 nanosheets as Fenton-like heterogeneous catalysts for degradation of salicylic acid, Chem. Eng. J. 333 (2018) 226–239.

[23] S.E. Sivan, K.H. Kang, S.J. Han, O.F.N. Okello, S.Y. Choi, V. Sudheeshkumar, R.W. J. Scott, H.J. Chae, S. Park, U.H. Lee, Facile MOF-derived one-pot synthetic approach toward Ru single atoms, nanoclusters, and nanoparticles dispersed on CeO_2 supports for enhanced ammonia synthesis, J. Catal. 408 (2022) 316–328.

[24] Y.F. Gu, T. Cai, X.H. Gao, H.Q. Xia, W. Sun, J. Zhao, Q.G. Dai, X.Y. Wang, Catalytic combustion of chlorinated aromatics over WO_x/CeO_2 catalysts at low temperature, Appl. Catal. B 248 (2019) 264–276.

[25] H. Huang, Q.G. Dai, X.Y. Wang, Morphology effect of Ru/CeO_2 catalysts for the catalytic combustion of chlorobenzene, Appl. Catal. B 158 (2014) 96–105.

[26] Y. Peng, K.Z. Li, J.H. Li, Identification of the active sites on CeO_2–WO_3 catalysts for SCR of NO_x with NH_3: An in situ IR and Raman spectroscopy study, Appl. Catal. B 140 (2013) 483–492.

[27] F.Y. Zhou, Q. Xin, Y.J. Fu, Z.S. Hua, Y. Dong, M.C. Ran, H. Song, S.J. Liu, R.Y. Qu, Y. Yang, X. Zhang, C.H. Zheng, X. Gao, Efficient catalytic oxidation of chlorinated volatile organic compounds over RuO_2-WO_x/$Sn_{0.2}Ti_{0.8}O_2$ catalysts: Insight into the Cl poisoning mechanism of acid sites, Chem. Eng. J. 464 (2023), 142471.

[28] J.J. Li, X.C. Mo, K. Zhang, Salamat Ali, Z. Liu, P. Cheng, Y.D. Li, K. Sun, Y.J. Fu, Y. R. Wang, E.Q. Xie, Ru modulates the catalytic activity of Pt to modify WO_3 nanowires for high-performance hydrogen sensing at near room temperature, Appl. Surf. Sci. 615 (2023), 156286.

[29] J.T. Zhang, X.N. Mao, S.L. Wang, L.L. Liang, M.F. Cao, L. Wang, G. Li, Y. Xu, X. Q. Huang, Superlattice in a Ru Superstructure for Enhancing Hydrogen Evolution, Angew. Chem. Int. Ed. 61 (2022), e202116867.

[30] L.C. Liu, A. Corma, Identification of the active sites in supported subnanometric metal catalysts, Nat. Catal. 4 (2021) 453–456.

[31] Z.R. Ma, D. Weng, X.D. Wu, Z.C. Si, Effects of WO_x modification on the activity, adsorption and redox properties of CeO_2 catalyst for NO_x reduction with ammonia, J. Environ. Sci. 24 (2012) 1305–1316.

[32] Q.X. Zhou, S.L. Ma, S.H. Zhan, Superior photocatalytic disinfection effect of Ag-3D ordered mesoporous CeO_2 under visible light, Appl. Catal. B 224 (2018) 27–37.

[33] F.C. Lu, S.Q. Guo, Z.P. Yang, Y.M. Yang, P.L. Li, X. Li, Q.L. Liu, Photoluminescence properties of $Y_5Si_3O_{12}N$: Ce^{3+} blue-emitting phosphors for white LED, J. Alloy. Compd. 521 (2012) 77–82.

[34] Z.Y. Chu, J.Q. Li, Y.P. Lan, C.Y. Chen, J. Yang, D.Y. Ning, X.W. Xia, X.S. Mao, KCl–LiCl molten salt synthesis of LaOCl/CeO_2-g-C_3N_4 with excellent photocatalytic-adsorbed removal performance for organic dye pollutant, Ceram. Int. 48 (2022) 15439–15450.

[35] X.Y. Xiong, Y.R. Jin, H.W. Wang, P. He, X. Xiang, P.C. Hu, K.F. Liu, Q.Q. Wei, B. Z. Wang, Study on the hydrogen production properties and electron transfer mechanism of CdS/WO_3 composite photocatalyst, Mater. Chem. Phy. 281 (2022), 125824.

[36] Y. Takamatsu, Y. Daiko, S. Kohara, K. Suzuya, A. Mineshige, T. Yazawa, The state of P═O_{nb} non-bridging oxygen and proton incorporation in binary MO·P_2O_5 (M= Ca, Mg) phosphate glasses, Solid. State Ion. 245 (2013) 19–23.

[37] Z.D. Shen, E.H. Gao, X.Y. Meng, J.C. Xu, Y. Sun, J.L. Zhu, J. Li, Z.L. Wu, W. Wang, S.L. Yao, Q.G. Dai, Mechanistic Insight into Catalytic Combustion of Ethyl Acetate on Modified CeO_2 Nanobelts: Hydrolysis–Oxidation Process and Shielding Effect of Acetates/Alcoholates, Environ. Sci. Technol. 57 (2023) 3864–3874.

[38] L. Wei, Y.X. Liu, H.X. Dai, S.P. Cui, C. Wang, H.C. Hsi, E. Duan, Y. Peng, J.G. Deng, Electronic structure tailoring of Al^{3+}– and Ta^{5+}– doped CeO_2 for the synergistic removal of NO and chlorinated organics, Appl. Catal. B 304 (2022), 120939.

[39] X. Xie, Y.X. Fan, W.Y. Tian, M. Zhang, J.L. Cai, X.G. Zhang, J. Ding, Y.S. Liu, S. Y. Lu, Construction of Ru/WO_3 with hetero-interface structure for efficient hydrogen evolution reaction, J. Energy Chem. 83 (2023) 150–157.

[40] F. Yang, S. Kundu, A.B. Vidal, J. Graciani, P.J. Ramirez, Sanjaya, D. Senanayake, D. Stacchiola, J. Evans, P. Liu, J.F. Sanz, J.A. Rodriguez, Determining the Behavior of RuO_x Nanoparticles in Mixed-Metal Oxides: Structural and Catalytic Properties of RuO_2/TiO_2(110), Surf. Angew. Chem. Int. Ed. 123 (2011) 10380–10384.

[41] D.Z. Chen, H.Y. Liu, J.M. Chen, Y. Yu, Enhancing bioelectrocatalytic oxidation of gaseous chlorobenzene by introducing transmembrane Ru^{4+}/Ru^{3+}-mediated reversible intracellular electron transfer, Appl. Catal. B 335 (2023), 122874.

[42] X.C. Cao, Y. Zhang, C.Y. Lu, L. Chen, X.J. Zheng, R.Z. Yang, Electronic structure modulation of Ru/$W_{20}O_{58}$ catalyst via interfacial Ru–O–W bridging bond for high-performance Li–O_2 batteries, Appl. Surf. Sci. 609 (2023), 155453.

[43] J.C. Ji, Y. Xu, Y. Liu, Y. Zhang, A nanosheet Ru/WO_3 catalyst for efficient conversion of glucose to butanediol, Catal. Commun. 144 (2020), 106074.

[44] N.X. Li, Y. Zheng, L.F. Wei, H.C. Teng, J.C. Zhou, Metal nanoparticles supported on WO_3 nanosheets for highly selective hydrogenolysis of cellulose to ethylene glycol, Green. Chem. 19 (2017) 682–691.

[45] J.D. Chen, C.H. Chen, M.K. Qin, B.B. Lin, Q. Mao, H.B. Yang, B. Liu, Y. Wang, Reversible hydrogen spillover in Ru-WO_{3-x} enhances hydrogen evolution activity in neutral pH water splitting, Nat. Commun. 13 (2022) 5382.

[46] J.Q. Zheng, K.Q. Yu, S.S. Yuan, L.J. Xiang, K.W. Wang, S.B. Jing, N. Li, Coupling Ru single-atom and oxygen vacancy in Ru/SnO_{2-x} for efficient nitrogen reduction to ammonia via electronic synergistic effect, J. Alloy. Compd. 962 (2023), 171028.

[47] L.N. Zhang, Z.L. Lang, Y.H. Wang, H.Q. Tan, H.Y. Zang, Z.H. Kang, G.Y. Li, Cable-like Ru/WNO@C nanowires for simultaneous high-efficiency hydrogen evolution and low-energy consumption chlor-alkali electrolysis, Energy Environ. Sci. 12 (2019) 2569–2580.

[48] S. Cao, H.Q. Wang, F.X. Yu, M.P. Shi, S. Chen, X.L. Weng, Y. Liu, Z.B. Wu, Catalyst performance and mechanism of catalytic combustion of dichloromethane (CH_2Cl_2) over Ce doped TiO_2, J. Colloid Interface Sci. 463 (2016) 233–241.

[49] J. Zhao, H.C. Zhang, H.Y. Wang, J.J. Wang, Tuning Lewis acid/base on the TiO_2-supported Pd-CoO_x interfaces to control the CO_2 selective hydrogenation, Mol. Catal. 518 (2022), 112076.

[50] W. Deng, Q.G. Dai, Y.J. Lao, B.B. Shi, X.Y. Wang, Low temperature catalytic combustion of 1, 2-dichlorobenzene over CeO_2–TiO_2 mixed oxide catalysts, Appl. Catal. B (181) (2016) 848–861.

[51] R. Farra, S. Wrabetz, M.E. Schuster, E. Stotz, N.G. Hamilton, A.P. Amrute, J. P. Ramírez, N. López, D. Teschner, Understanding CeO_2 as a Deacon catalyst by probe molecule adsorption and in situ infrared characterisations, Phys. Chem. Chem. Phys. 15 (2013) 3454–3465.

[52] Q.G. Dai, S.X. Bai, H. Li, W. Liu, X.Y. Wang, G.Z. Lu, Catalytic total oxidation of 1,2-dichloroethane over highly dispersed vanadia supported on CeO_2 nanobelts, Appl. Catal. B 168 (2015) 141–155.

[53] X.H. Yu, L.Y. Dai, J.G. Deng, Y.X. Liu, L. Jing, X. Zhang, R.Y. Gao, Z.Q. Hou , L. Wei, H.X. Dai, An isotopic strategy to investigate the role of water vapor in the oxidation of 1,2-dichloroethane over the Ru/WO_3 or Ru/TiO_2 catalyst, Appl. Catal. B 305 (2022), 121037.
[54] F.W. Lin, Z.M. Zhang, N. Li, B.B. Yan, C. He, Z.P. Hao, G.Y. Chen, How to achieve complete elimination of Cl-VOCs: A critical review on byproducts formation and inhibition strategies during catalytic oxidation, Chem. Eng. J. 404 (2021), 126534.
[55] P.F. Sun, S.Y. Zhai, J.K. Chen, J.L. Yuan, Z.B. Wu, X.L. Weng, Development of a multi-active center catalyst in mediating the catalytic destruction of chloroaromatic pollutants: A combined experimental and theoretical study, Appl. Catal. B 272 (2020), 119015.
[56] X.H. Yu, L.Y. Dai, Y. Peng, J.G. Deng, Y.X. Liu, L. Jing, X. Zhang, Z.Q. Hou, J. Wang, H.X. Dai, High Selectivity to HCl for the Catalytic Removal of 1, 2-Dichloroethane Over RuP/3DOM WO_x: Insights into the Effects of P-Doping and H_2O Introduction, Environ. Sci. Technol. 55 (2021) 14906–14916.
[57] Q.G. Dai, W. Wang, X.Y. Wang, G.Z. Lu, Sandwich-structured CeO_2@ZSM-5 hybrid composites for catalytic oxidation of 1, 2-dichloroethane: An integrated solution to coking and chlorine poisoning, Appl. Catal. B 203 (2017) 31–42.
[58] H. Wang, B. Peng, R.D. Zhang, H.X. Chen, Y. Wei, Synergies of Mn oxidative ability and ZSM-5 acidity for 1, 2-dichloroethane catalytic elimination, Appl. Catal. B 276 (2020), 118922.
[59] X.H. Yu, J.G. Deng, Y.X. Liu, L. Jing, R.Y. Gao, Z.Q. Hou, Z.X. Zhang, H.X. Dai, Enhanced Water Resistance and Catalytic Performance of Ru/TiO_2 by Regulating Brønsted Acid and Oxygen Vacancy for the Oxidative Removal of 1, 2-Dichloroethane and Toluene, Environ. Sci. Technol. 56 (2022) 11739–11749.
[60] L. Zhang, W. Deng, Y.P. Cai, Q.G. Dai, L.M. Guo, Comparative Studies of Phosphate-Modified CeO_2 and Al_2O_3 for Mechanistic Understanding of Dichloromethane Oxidation and Chloromethane Formation, ACS Catal. 10 (2020) 13109–13124.